

ASAR imaging for coastal upwelling in the Baltic Sea

Igor E. Kozlov^{a,b,f,*}, Vladimir N. Kudryavtsev^{a,b}, Johnny A. Johannessen^{c,d},
Bertrand Chapron^e, Inga Dailidienė^f, Alexander G. Myasoedov^{a,b}

^a Russian State Hydrometeorological University, 98, Malookhtinsky prospect, 195196 St. Petersburg, Russian Federation

^b Nansen International Environmental and Remote Sensing Centre, 7, 14th line, 199034 St. Petersburg, Russian Federation

^c Nansen Environmental and Remote Sensing Centre, Thormøhlensgate 47, N-5006 Bergen, Norway

^d Geophysical Institute, University of Bergen, Allégaten 70, N-5000 Bergen, Norway

^e Institut Français de Recherche pour l'Exploitation de la Mer, BP 70, 29280 Plouzane, France

^f Department of Geophysical Sciences, Klaipėda University, H. Manto g. 84, LT-92291 Klaipėda, Lithuania

Available online 26 August 2011

Abstract

Analysis of Envisat Advanced Synthetic Aperture Radar (ASAR) and Aqua/Terra Moderate Imaging Spectrometer (MODIS) infrared (IR) imagery of coastal upwelling in the southeastern Baltic Sea is presented. It is found that upwelling features are well distinct in the SAR images, and the leading imaging mechanism appears to be the change of the marine atmospheric boundary layer (MABL) stratification over the sea surface temperature (SST) front. This finding is supported by model calculations of the MABL transformation supplemented with the SAR backscatter calculations based on the CMOD4 model. In addition an empirical dependence of the SAR contrasts over the upwelling region on the wind speed and the SST drop is suggested. Finally, surface slicks accumulated in the sea surface current convergence zones generate additional distinct features in SAR imagery. This effect is interpreted within the framework of the coastal current circulation model based on analysis of the SST snapshot.

© 2011 COSPAR. Published by Elsevier Ltd. All rights reserved.

Keywords: Coastal upwelling; SAR imaging; MABL transformation over temperature front; Surface slicks; The Baltic Sea

1. Introduction

Coastal upwelling is a well known and important dynamical feature in the Baltic Sea (Lehmann and Myrberg, 2008). In cloud free conditions satellite optical and infrared imagery have demonstrated their high efficiency for investigation of the upwelling dynamics (Bychkova and Viktorov, 1987; Siegel et al., 2006; Suursaar and Aps, 2007; Uibopin and Laanemets, 2009), and these products are now routinely used in operational oceanography.

However frequent cloud cover is typical for this area (Krežel et al., 2005), and hence the opportunity to use satellite synthetic aperture radar (SAR) data (which are independent on cloud and illumination conditions) is explored for investigation of coastal upwelling as well as other upper ocean phenomena (Beal et al., 1981; Johannessen et al., 1991, 1996; Johannessen, 2000). Quantification of the SAR data in terms of the sea surface temperature (SST) frontal characteristics (e.g. location and extent of the front, SST drop over the front) might be of high practical interest for a variety of oceanographic applications.

The ability of the SAR to monitor sea surface frontal zones (including the SST fronts) is justified by a number of physical factors, such as: transformation of the sea surface roughness due to wave-current interactions (Johannessen et al., 1991; Marmorino et al., 1994; Kudryavtsev et al., 2005) effect of the MABL transformation over the SST front (Kudryavtsev et al., 1996; Beal et al., 1997; Kudryavtsev

* Corresponding author at: Russian State Hydrometeorological University, 98, Malookhtinsky prospect, 195196 St. Petersburg, Russian Federation.

E-mail addresses: igor.eko@gmail.com (I.E. Kozlov), vladimir.kudryavtsev@niersc.spb.ru (V.N. Kudryavtsev), johnny.johannessen@niersc.no (J.A. Johannessen), bertrand.chapron@ifremer.fr (B. Chapron), inga.dailidienė@ku.lt (I. Dailidienė).

et al., 1999) and accumulation of surfactants and suppression of waves in the convergence zone (Clemente-Colon and Yan, 2000; Espedal et al., 1998; Johannessen et al., 2005). All these factors are very relevant to the nature of the upwelling phenomena, and their combined effect may significantly complicate and challenge the interpretation of thermal front expressions in SAR images (Johannessen et al., 2005).

The main goal of this study is to interpret SAR signatures of an upwelling event in the southeastern Baltic Sea in July 2006 and to identify the governing mechanisms responsible for its surface manifestation. In Section 2 the data and the approach is addressed, while the presentation of the simulation of the SAR imaging capabilities of the upwelling event follows in Section 3. Section 4 then contains the discussion of the results followed by the conclusion in Section 5.

2. Data and approach

Upwelling of the cold nutrient-rich waters in the southeastern Baltic Sea during the summer period is a typical phenomenon regularly observed in both *in situ* and satellite data (Bychkova and Viktorov, 1987; Kowalewski and Ostrowski, 2005; Zhurbas et al., 2004). In this part of the Baltic Sea upwelling development is favored by northerly winds blowing parallel to the coast (Bychkova and Viktorov, 1987). Under the strongly stratified conditions, which usually are the case for midsummer period, even relatively weak winds can lead to upwelling intensification (Lehmann and Myrberg, 2008).

In this study we focus our analysis on Envisat ASAR images supplemented with Aqua/Terra MODIS IR data and *in situ* measurements from coastal hydrometeorological stations along the SE Baltic Sea coast (Fig. 1). The Envisat ASAR C-band (5.6 cm) images used in the study were acquired at vertical polarization and Wide Swath Mode (WSM) with spatial resolution of 150 m. Supplementary SST maps were obtained from Aqua/Terra MODIS L2 data with spatial resolution of about 1 km (Brown and Minnett, 1999). The wind information was derived from the corresponding ASAR images (hereinafter, SAR wind) using the CMOD4 model function (Stoffelen and Anderson, 1997) with the input wind direction obtained from the NCEP GFS 0.5 degree 6-hourly wind forecast (http://nomad5.ncep.noaa.gov/ncep_data/index.html).

2.1. Upwelling observations

According to the meteorological data from the coastal stations favorable northerly upwelling triggering winds (from 5 m/s and higher) were observed in the study region from 12 to 17 July 2006 (noted as “F” in Fig. 1(b)).

Starting on 15 July 2006 the upwelling event was imaged by seven consecutive ASAR acquisitions during a 2 weeks period. In this study the analysis is restricted to two of

these SAR images containing a variety of the frontal expressions. Figs. 2 and 3 show the coastal upwelling signatures in concurrent Envisat ASAR normalized radar cross section (NRCS), MODIS SST and SAR wind data for 16 and 19 July 2006.

The map of MODIS SST acquired on 16 July 2006 at 19:40 UTC depicts the presence of a “narrow” area of cold waters adjacent to the coastline (Fig. 2(b)). A strong 10–12 °C SST drop between the ambient and upwelling waters is clearly seen. At the time of the image acquisition the upwelling front is perturbed by the development of several transverse filaments possibly resulting from the interaction of a longshore baroclinic jet current with bottom topography as suggested by Zhurbas et al. (2004). The coincident wind conditions are characterized by north-northeasterly winds of 4–6 m/s (Fig. 2(c)). The SAR image acquired on the same day at 20:05 UTC (Fig. 2(a)) manifests the presence of dark features that are correlated with the location of the cold upwelling waters as well as the offshore elongated filaments. However, the magnitude of the NRCS contrast along the upwelling front is not uniform; in its lower part (55N–56N) the NRCS drop is rather weak at about 1–1.5 dB, whereas in its upper part (56N–57.3N) it reaches up to 7–8 dB.

On July 17 the wind direction deviates from the upwelling favorable northerly winds (see Fig. 1(b)), and the upwelling dynamics gradually relax followed by development of meandering features and eddies along the frontal boundary (see Fig. 3). On 19 July 2006 the MODIS SST and ASAR images were acquired with a 1 min time separation. The SAR wind field in this case exhibits the presence of an atmospheric front that intercepts the upwelling area (Fig. 3(c)). This wind front appears to be partly accompanied by a 50 km wide band of clouds that mask the thermal expressions in the SST map in a northwesterly direction (see Fig. 3(b)). In the upper part of the SAR image (56N–57.3N) the northeasterly winds range from 4 to 6 m/s whereas the lower part of the SAR image (54.8N–56N) is characterized by light winds. In result the southern region reveal distinct expressions of upwelling features and meanders in the SAR backscatter patterns (Fig. 3(a)) with modulations up to 7–10 dB accompanied by MODIS SST fronts of about 5–7 °C. In the area north of the front the more gentle SST changes of 3–5 °C result in weaker NRCS modulation of up to 1.5 dB. Unlike the SST data affected by clouds, the SAR image still provides valuable manifestation on the thermal front location although with relatively weak NRCS contrasts.

In the SAR image one may also notice some additional dark patterns (e.g. 55.5N 20E) which are not coincident with the position of the upwelling front. These are likely associated with the manifestation of surfactant films in the low wind speed area and will be further discussed in Section 4. In the next sub-section we address the role of the MABL for the SAR image expression of the upwelling features.

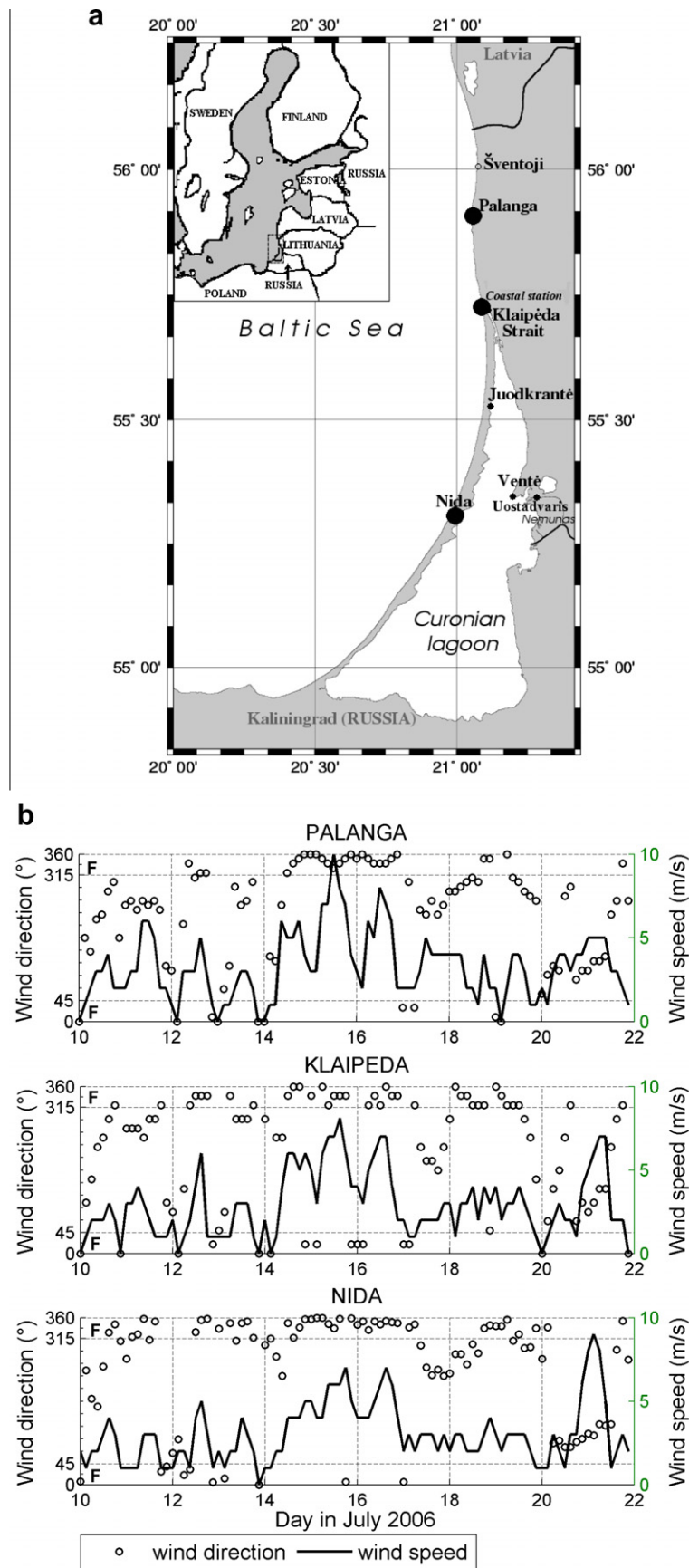


Fig. 1. (a) Map of the SE Baltic Sea with the location (black points) of three Lithuanian coastal stations. (b) Wind field records at the coastal stations before and during coastal upwelling event in July 2006.

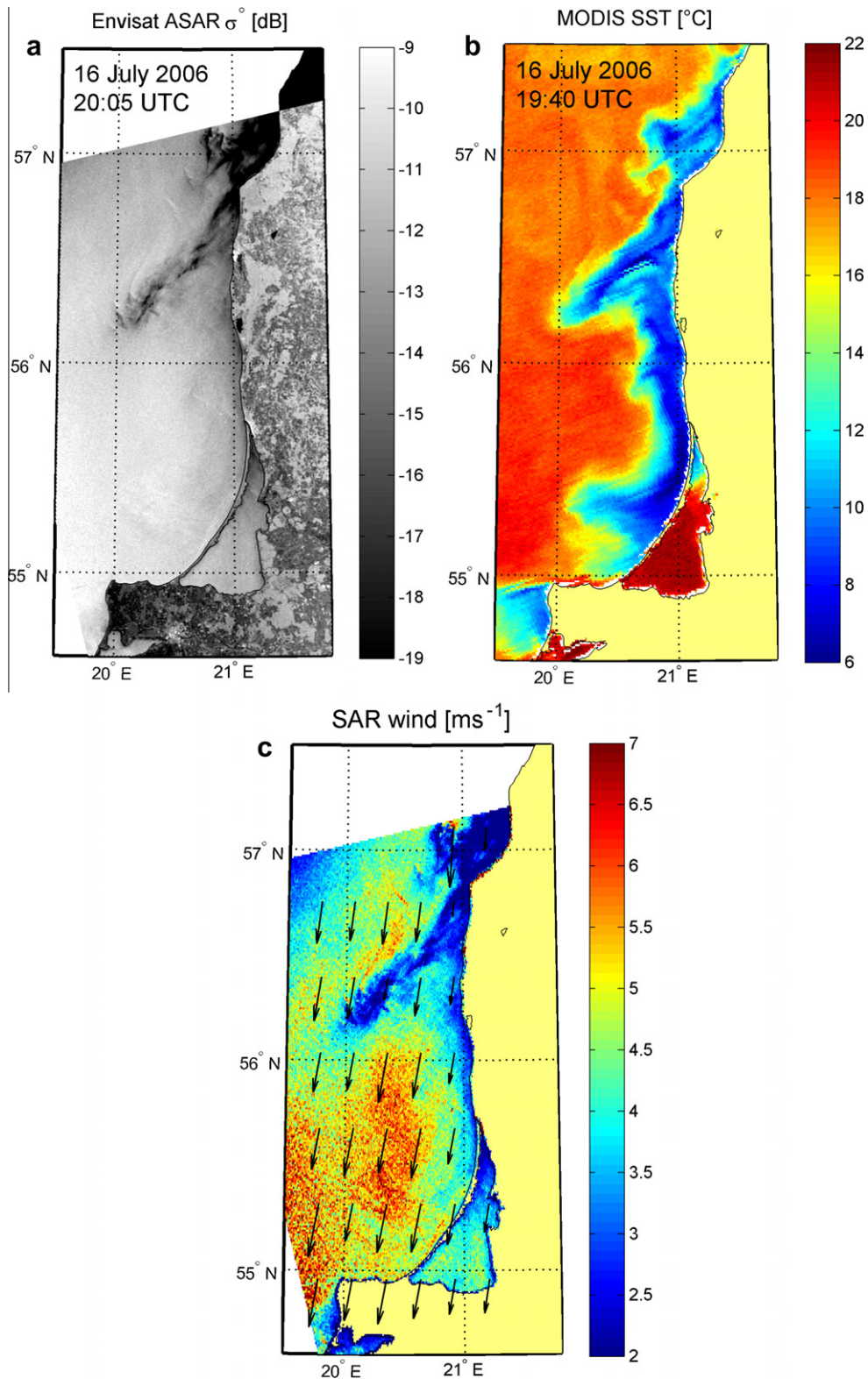


Fig. 2. Upwelling manifestation on 16 July 2006 in concurrent (a) Envisat ASAR (© ESA) NRCS, (b) MODIS Terra (© NASA) SST and (c) SAR derived near surface wind speed fields. Envisat ASAR image acquired on 16 July 2006 at 20:05 UTC. MODIS image acquired on 16 July 2006 at 19:40 UTC. Arrows in (c) indicate wind direction derived from the NCEP model.

2.2. Role of the MABL on SAR imaging of upwelling front

The SST fronts affect the stratification in the MABL and subsequently the near-surface wind speed and surface stress

(Askari et al., 1993; Kudryavtsev et al., 1996). Since the wind stress predetermines the short wind wave spectrum it also therefore strongly influence the radar backscattering, e.g. enhanced radar backscatter is usually associated

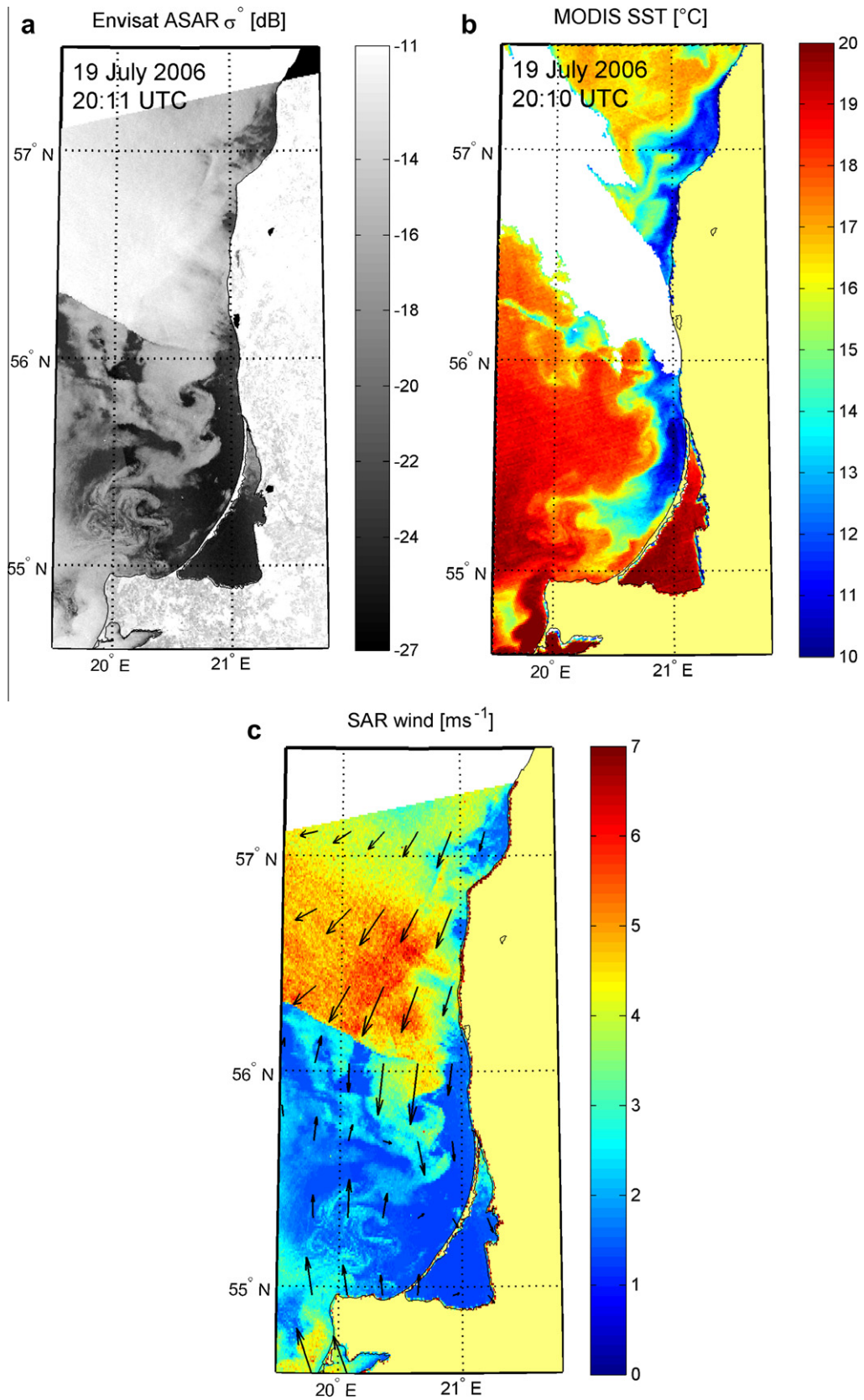


Fig. 3. Upwelling manifestation on 19 July 2006 in concurrent. (a) Envisat ASAR (© ESA) NRCS, (b) MODIS Terra (© NASA) SST and (c) SAR derived near surface wind speed fields. Envisat ASAR image acquired on 19 July 2006 at 20:11 UTC. MODIS image acquired on 19 July 2006 at 20:10 UTC. Arrows in (c) indicate wind direction derived from the NCEP model. Note that the ASAR noise equivalent σ° is about -24 dB.

with the warm side of the SST fronts (unstable MABL), while the suppression in the backscatter occurs at the cold side (stable MABL) (Askari et al., 1993; Beal et al., 1997; Kudryavtsev et al., 1996; Weissmann et al., 1980).

In order to assess the effect of the MABL transformation across the upwelling zone on the SAR backscatter variations, we assume that: (i) the scale of the spatial variations of the geostrophic wind speed and the temperature of the free atmosphere (at the height of order of 1 km) is much larger than the spatial scale of the upwelling; and (ii) the vertical structure of the MABL across the front is fully adjusted to the local SST. In this case the resistance law for the planetary MABL relating the surface wind stress (friction velocity) to the geostrophic wind speed and the stratification parameter takes the standard form and reads:

$$\frac{\kappa \mathbf{G}}{\mathbf{u}_*} = \ln(\kappa \mathbf{u}_* / f z_0) - B(\mu) - iA(\mu), \quad (1)$$

where $\kappa = 0.4$ is the von Karman's constant, μ is the stratification parameter, f is the Coriolis parameter, $\mathbf{G} = G \exp(i\varphi_G)$ is the (complex) geostrophic wind velocity with direction φ_G , $\mathbf{u}_* = u_* \exp(i\varphi_w)$ is the (complex) surface friction velocity, φ_w the direction of the near-surface wind, and $A(\mu)$, $B(\mu)$ are universal dimensionless functions for the planetary MABL. z_0 is the surface roughness scale defined as a composition of the roughness scale for the smooth surface and aerodynamically rough surface (e.g. Smith, 1988) such that:

$$z_0 = 0.1 \cdot \nu / u_* + 0.015 \cdot g / u_*^2, \quad (2)$$

where ν is the air viscosity coefficient and g is the gravity acceleration. For practical applications the stratification parameter μ can be estimated through the following bulk relation (Kudryavtsev et al., 1996)

$$\mu = \kappa^2 (g / T_K) (\theta_a - \theta_s) / fG, \quad (3)$$

where θ_a is the potential air temperature at the upper boundary of the planetary MABL, θ_s is the sea surface temperature, (g / T_K) is a buoyancy parameter, where $T_K = 300 \text{ °K}$ is the mean MABL temperature in our case. In the present study we specified the universal dimensionless functions $A(\mu)$ and $B(\mu)$ following the simplified two-layer model for the planetary atmospheric boundary layer suggested by Brown (1982, his Eqs. (13) and (14)). If the surface friction velocity is found from the resistance law (Eq. (1)), then the equivalent wind speed for the neutrally stratified MABL at standard 10-m level, U_{10} (the input parameter for CMOD4 calculations), is

$$U_{10} = u_* / \kappa \cdot \ln(10 / z_0). \quad (4)$$

Thus Eqs. (1) and (4) define the surface friction velocity and the wind speed at the reference level for the specified parameters of the free atmosphere (\mathbf{G} and θ_a) and the surface temperature θ_s which can vary in space.

The procedure for the model calculations has been organized in the following steps:

- First, outside the upwelling region the background SAR wind speed U_{10} is determined using the CMOD4 algorithm (Stoffelen and Anderson, 1997) with a priori specified wind direction taken from NCEP.
- Secondly, the background friction velocity $\bar{u}_* = C_d^{1/2} U_{10}$ is determined with the surface drag coefficient defined as $C_d = [\kappa / \ln(10 / z_0)]^2$.
- Following this the geostrophic wind is estimated from the inversion of the resistance law (Eq. (1)) where the potential temperature at the top of the planetary MABL θ_a is assumed equal to the mean $\bar{\theta}_s$ outside the upwelling region, i.e. implying that the background MABL is assumed to be neutrally stratified.
- Subsequently these fields (the geostrophic wind velocity, the air temperature θ_a , and the observed surface temperature $\theta_s(x, y)$) are used to calculate the surface friction velocity $u_*(x, y)$ in the upwelling area following the resistance law expressed in Eq. (1) combined with Eq. (3).
- Finally, the modified wind speed over the upwelling zone at standard 10-m level is calculated from Eq. (4), which, in turn, is invoked into the CMOD4 model for estimation of the radar backscatter.

3. Model analysis of upwelling manifestation in SAR

The approach outlined in the previous section is then used to interpret the observed expressions of the upwelling features in the SAR images on 16 and 19 July 2006.

The background 10-m wind speed map derived from the SAR data on 16 July 2006 is shown in Fig. 4(a). In comparison, the predicted wind speed map influenced by the upwelling zone is shown in Fig. 4(b). As noticed the wind speed over the cold water in the upwelling region drops as the MABL stratification turns stable. This is in general agreement with SAR wind field displayed in Fig. 2(c). However, inside the upwelling zone the predicted wind speed seems to partly overestimate the depression.

Invoking the wind field displayed in Fig. 4(b) into the CMOD4 the corresponding retrieval of the radar backscatter as shown in Fig. 5(a) can be compared to the observed SAR image shown in Fig. 5(b). Both maps are presented in terms of the NRCS contrast $K_{\sigma} = (\sigma^\circ - \bar{\sigma}^\circ) / \bar{\sigma}^\circ$, where in order to remove the range trend, the mean $\bar{\sigma}^\circ$ is defined as the NRCS averaged in the azimuth direction. Overall the simulated backscatter displays a large scale pattern in agreement with the observed. However, the simulated backscatter patterns of the upwelling features are more distinct as a result of the overestimation of the wind speed suppression in the upwelling region. Fig. 6 shows a scatter diagram of modeled and observed SAR contrasts. The correlation coefficient is $R = 0.46$, implying that the simulation model, in general, is consistent with observations, with the best correlation found in the upper part of the SAR image (north of 56N).

In the 19 July 2006 case the background 10-m wind speed derived from the ASAR is shown in Fig. 7(b). In this

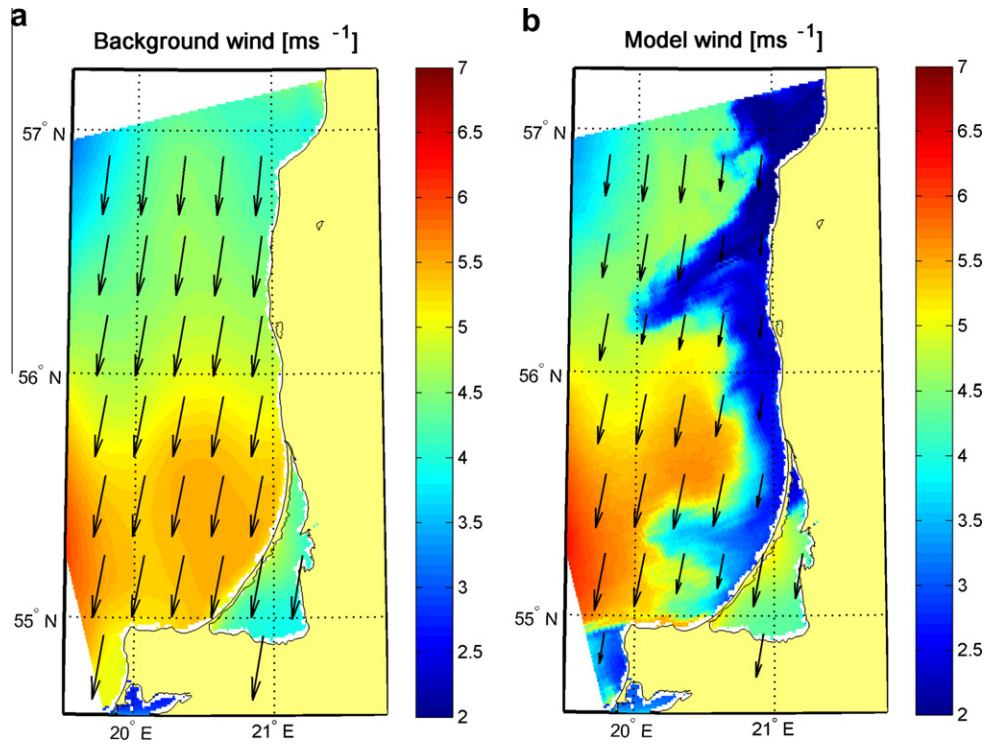


Fig. 4. (a) The background SAR wind field used to initialize the MABL model [m/s]. (b) Modeled near-surface wind speed as affected by the upwelling zone [m/s].

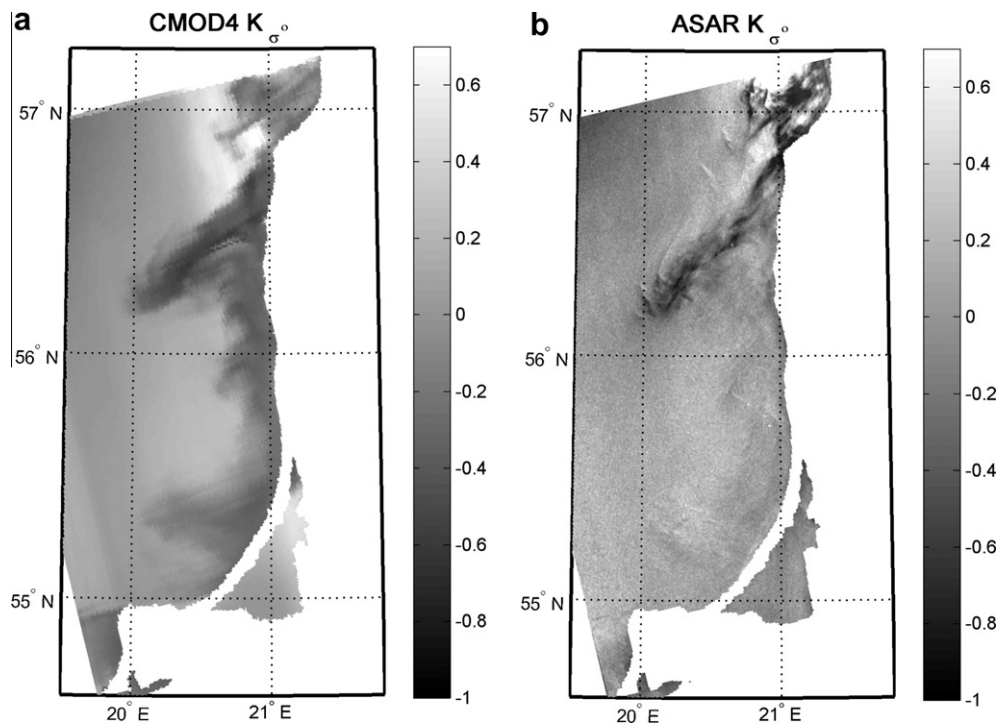


Fig. 5. (a) Simulated and (b) observed NRCS contrasts for the 16 July 2006 event.

case the study area was partly covered by the clouds. Therefore, in order to reconstruct the SST field for the entire area, a composite SST field (see Fig. 7(a)) is created combining the concurrent MODIS image (Fig. 3(b)) with

the nearest images obtained on 19 July at 01:10 and 10:45 (UTC). Fig. 7(c) shows the corresponding output wind field from the MABL model. All in all the predicted wind speed is in good agreement with the SAR wind field

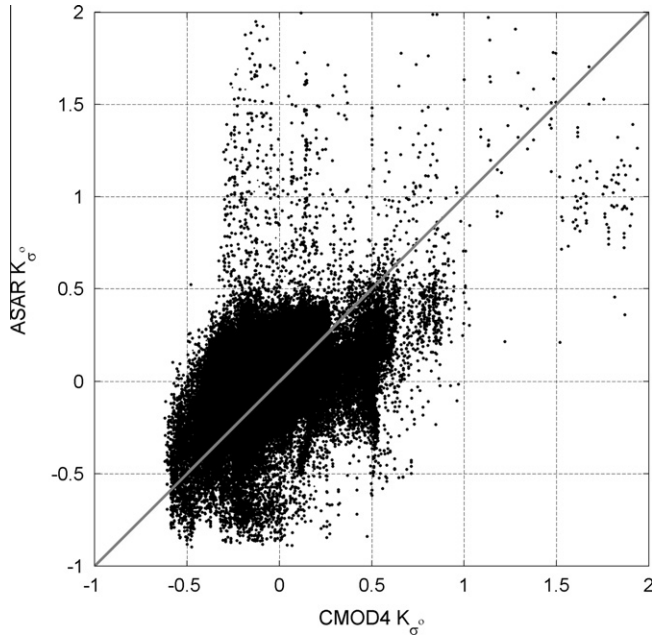


Fig. 6. Scatter diagram of the model (CMOD4) NRCS contrasts versus the observed Envisat ASAR NRCS contrasts for the 16 July 2006 event.

shown in Fig. 3(c). However, as in the previous case, the effect of the stratification on the MABL dynamics results in a significant suppression of the wind speed over the cold upwelling waters.

The comparison between the simulated and observed SAR images is shown in Fig. 8 and reveals a very good quantitative agreement in the backscatter pattern associated with the upwelling features. Further evidence of this is depicted in the scatter plot shown in Fig. 9 with a correlation coefficient of $R = 0.89$. The best correspondence between the model and the observations is found in the low wind speed area (south of 56N), especially between 55N and 55.5N where the wind speed is about 2–3 m/s (see Fig. 3(c)). As emphasized in Section 2.2, this area is characterized by a good agreement in the spatial patterns of the SAR and the SST anomalies (see Fig. 3). This may be explained by the fact that at low winds the radar signal is close to the threshold level, thus any additional decrease of the wind speed coming from changes in the MABL stratification over the cold front can lead to further drop of the radar backscatter below the noise floor. This is exactly what the model suggests in Fig. 8(a).

However, some discrepancies between the simulated and the observed SAR image expressions are also evident. In particular, some of the dark patterns observed in the SAR image (the area around 55.5N 20E) are not adequately reproduced in the model. This might imply that their origin cannot be entirely explained by the impact of stratification changes. Since the NRCS is also sensitive to the presence of surfactants at low winds (Espedal et al., 1998), it might be anticipated that the dark SAR patterns, which are not correlated with the SST anomalies, might be caused by surfactant films.

Using all the seven Envisat ASAR images, the dependence of the NRCS contrasts $\Delta\sigma^\circ = \sigma^\circ - \bar{\sigma}^\circ$ (in dB) on the wind speed and the SST drop across the front can be further investigated from the relationship of the $\Delta\sigma^\circ$ to the dimensionless stratification parameter $\mu_f = \kappa^2(g/T_K) \cdot \Delta\theta_s/fU_{10}$ (see Fig. 10). Here the temperature change across the front is $\Delta\theta_s = \theta_s - \bar{\theta}_s$ and the input U_{10} and $\Delta\theta_s$ values for these ASAR data ranged between 2.5–8.5 m/s and 2–12 °C, respectively.

The squares in Fig. 10 display the dependence of $\Delta\sigma^\circ$ on μ_f as derived from the ASAR observations. The model simulations were calculated for the SST drops ranging from $\Delta\theta_s = 0$ °C to $\Delta\theta_s = -15$ °C combined with the neutral ($\theta_a - \bar{\theta}_s = 0$ °C) and unstable ($\theta_a - \bar{\theta}_s = -2$ °C) stratified MABL and the wind speeds U_{10} of 3 and of 6 m/s.

The data can be parameterized by the following empirical relation:

$$\Delta\sigma^\circ = a|\mu_f|^4/(1 + b|\mu_f|^4), \quad (5)$$

where $a = -8.1 \times 10^{-6}$ and $b = 10^{-6}$. Overall, the empirical relationship fit the observation data very well suggesting that the maximum suppression of the SAR backscatter (~ -10 dB) in the cold water sector might originate from the effect of the MABL transformation over the SST front. The validity of this empirical relation is limited to the local conditions during the observation periods. However, the underlying physics has no regional restriction, and the relationship expressed in Eq. (5) can therefore also be applied for other areas and conditions.

The question then arises when the SAR detection of the SST front is feasible. If one suggests that the NRCS drop over the front by factor 2 represents a criterion for reliable detection of the SST front by SAR, then referring to Fig. 10 one may find that such criterion is fulfilled if the parameter $\mu_f < -50$. This condition can be realized, for example, for SAR imaging of the SST front with $\Delta\theta_s = [-10; -5; -2]$ °C at winds less than $U_{10} = [9; 4.5; 1.8]$ m/s respectively. Hence, the SAR manifestations of the SST fronts associated with coastal upwelling is restricted by low to moderate wind speed conditions.

In addition, the sensitivity of the SAR imaging depends on the stratification of the MABL over the upwind sector of the front. The best sensitivity takes place if the MABL stratification on the upwind side of the front is weakly unstable. In this case the airflow crossing the SST front changes its stratification from unstable to stable, that, in turn, results in the highest response of the surface wind stress (and thus SAR signal) to the SST, as demonstrated by the model simulation with the triangles displayed in Fig. 10.

4. Discussion

The model simulations clearly suggest that the changes in the atmospheric boundary layer stratification over the marine thermal front are indeed one of the main causes

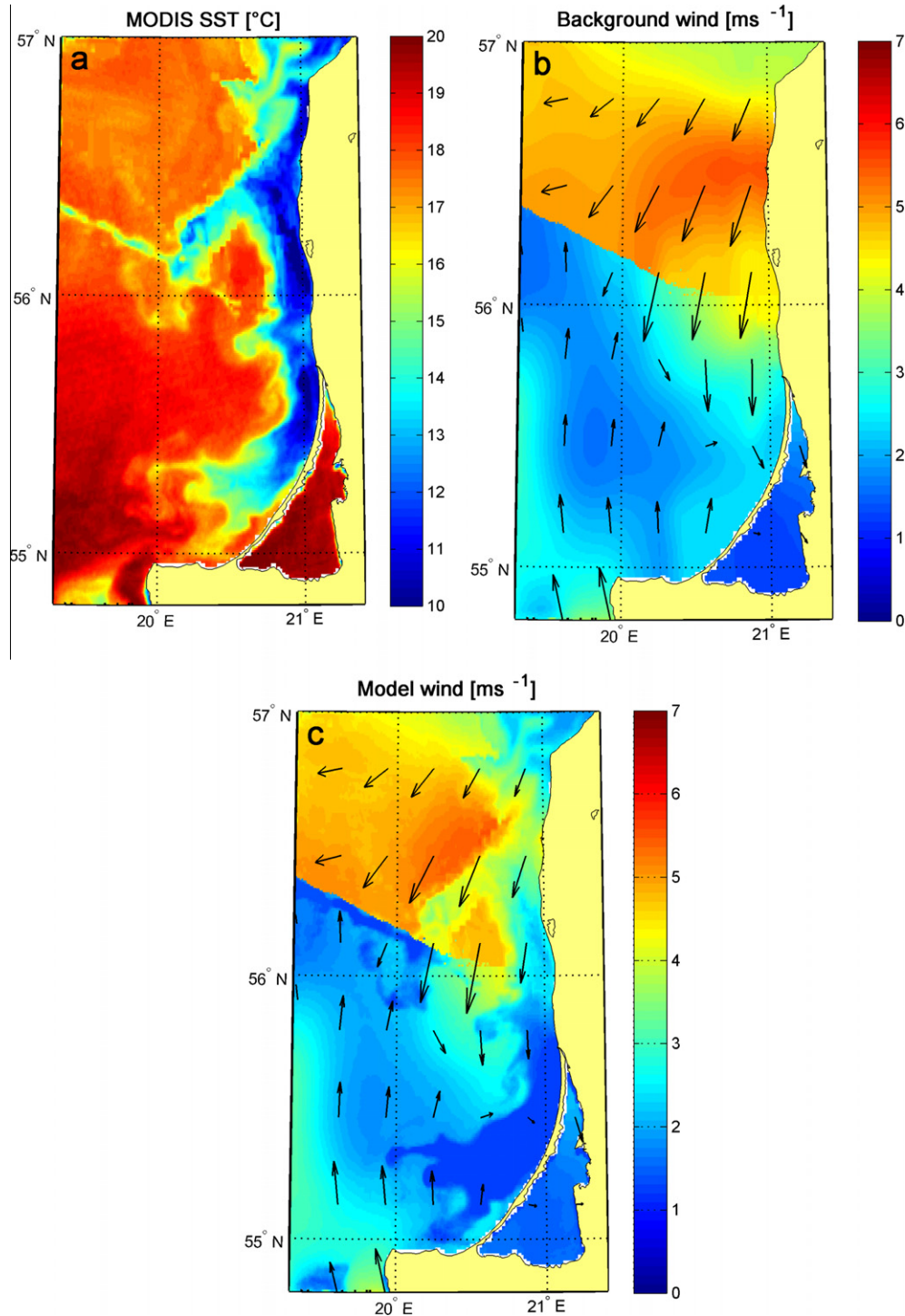


Fig. 7. (a) Mosaic of the MODIS SST [$^{\circ}\text{C}$]; (b) the background near-surface wind field [m/s]; (c) the simulated near-surface wind field for the 19 July 2006 event.

for the SAR imaging of the upwelling events, although the results contain some under- and overestimations of wind speed suppression over the cold upwelling waters. This may presumably be caused by shortcoming of the model approach which is based on the assumption that the MABL over the front is in an equilibrium state.

Moreover, the small-scale dark features observed inside the larger-scale dark patterns may be caused by the presence of surfactant films affecting the NRCS through damping of short wind waves. Fig. 11 shows an enlarged fragment of the SAR image on July 19 depicting the dark small-scale elongated features presumably associated with

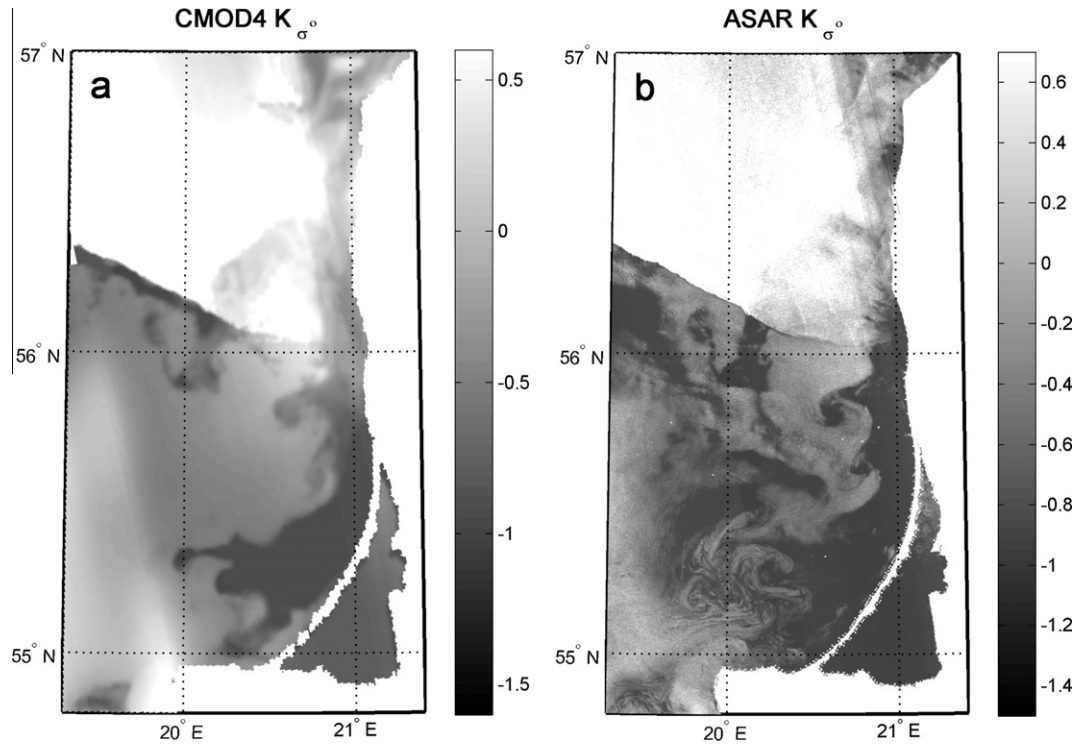


Fig. 8. (a) Simulated and (b) observed NRCS contrasts for the 19 July 2006 event.

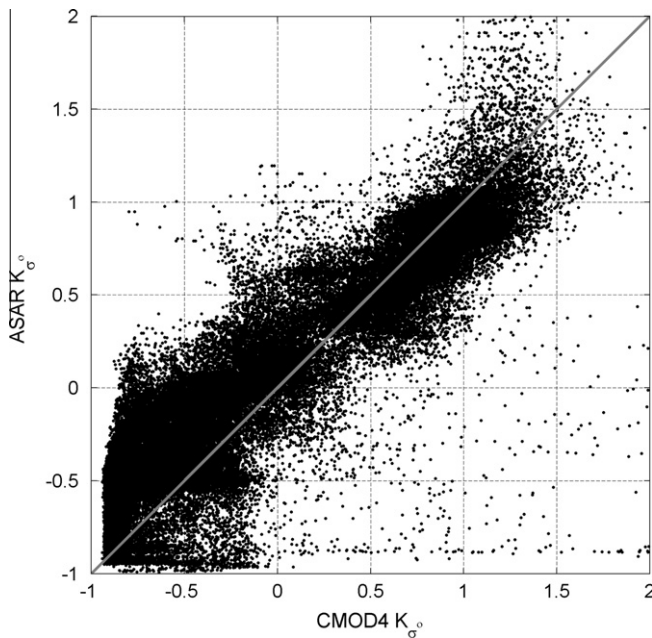


Fig. 9. Scatter diagram of the model (CMOD4) NRCS contrasts versus the observed Envisat ASAR NRCS contrasts for the 19 July 2006 event.

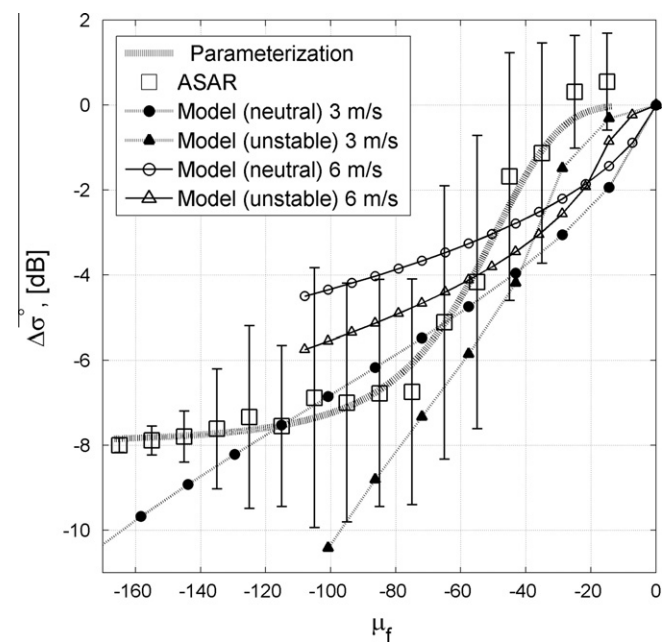


Fig. 10. The radar backscatter drop over the upwelling front as a function of the background wind speed and cross-front SST change. The ASAR observations are plotted as open squares with vertical bars representing the standard deviations; the model simulations are given for neutral (circles) and unstable (triangles) background MABL stratification and with a wind speed of 3 m/s (solid symbols) and of 6 m/s (open symbols). The bold dotted line is the parameterization of the averaged ASAR observations as determined from Eq. (5).

the accumulation of the surfactants in the zones of surface current convergence associated with meso- and sub-meso-scale upper ocean dynamics.

In order to interpret these features further the approach outlined by Kudryavtsev et al. (2010) and further substantiated in Kudryavtsev et al. (submitted for publication) for

the analysis and simulation of the SAR signatures of meso-scale current is followed. This approach capitalizes on the

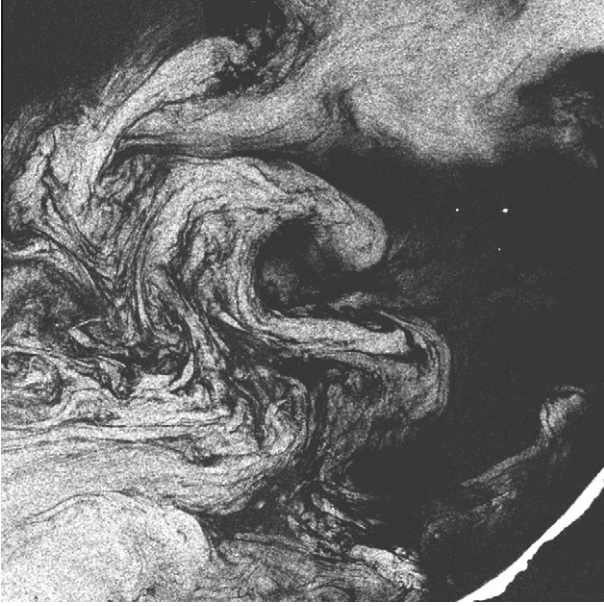


Fig. 11. A subscene of 19 July 2006 Envisat ASAR image depicting the narrow dark elongated bands of low radar backscatter presumably associated with short wave damping in the presence of surfactant films. (© ESA).

model findings by Isern-Fontanet et al. (2008) for the reconstruction of the surface quasi-geostrophic (SQG) currents from satellite infrared SST snapshot, and the model for the interaction of the Ekman currents with SQG current suggested by Klein and Hua (1990). The latter model describes the generation of the secondary ageostrophic current associated with the surface current convergence/divergence as:

$$\nabla \cdot \mathbf{V} = -f^{-1} \bar{u}_j \frac{\partial}{\partial x_j} \Omega_z, \quad (6)$$

where \bar{u}_j is the component of the Ekman drift current vector defined as $u = [\tau_2/(fh), -\tau_1/(fh)]$, τ_j is the wind stress scaled by the water density, f is the Coriolis parameter, h is the mixed layer depth, and Ω_z is the vorticity of the SQG currents. The vorticity can then, in turn, be defined through the SST field assuming that the effects of salinity on the density field can be ignored. In the Fourier space (variables are denoted by hat) the relationship between $\hat{\Omega}_z$ and $\hat{\theta}_s(\mathbf{k})$ reads:

$$\hat{\Omega}_z(\mathbf{k}) = \frac{g\alpha}{fn_b k} k^2 \hat{\theta}_s(\mathbf{k}), \quad (7)$$

where α is the thermal expansion coefficient of the surface density, k is the wave number, and n_b is the Prandtl number (see Isern-Fontanet et al. (2008) for more details). In order to calculate the surface current divergence field following from Eq. (6) with Eq. (7) we used the MODIS SST field (Fig. 2(b)) and the SAR derived wind speed field (Fig. 2(c)) as input parameters. The corresponding surface current divergence field calculated for the northern region with a mean wind speed of 5.5 m/s is shown in Fig. 12 together with the corresponding radar backscatter map. Comparing the expressions in the ASAR image (Fig. 12(a)) with the reconstructed surface current divergence field (Fig. 12(b)) a distinct similarity between the elongated dark/bright SAR patterns and the zones of surface current convergence/divergence is revealed. This suggests that the observed dark features in the SAR image are presumably linked to the zones of surface current convergence where the natural surface films suppressing short wind waves are accumulated. Thus the combined effect of the MABL transformation over the SST front and the impact of the surfactants on short wind waves, which can be typical for the summer conditions in the Baltic Sea, may

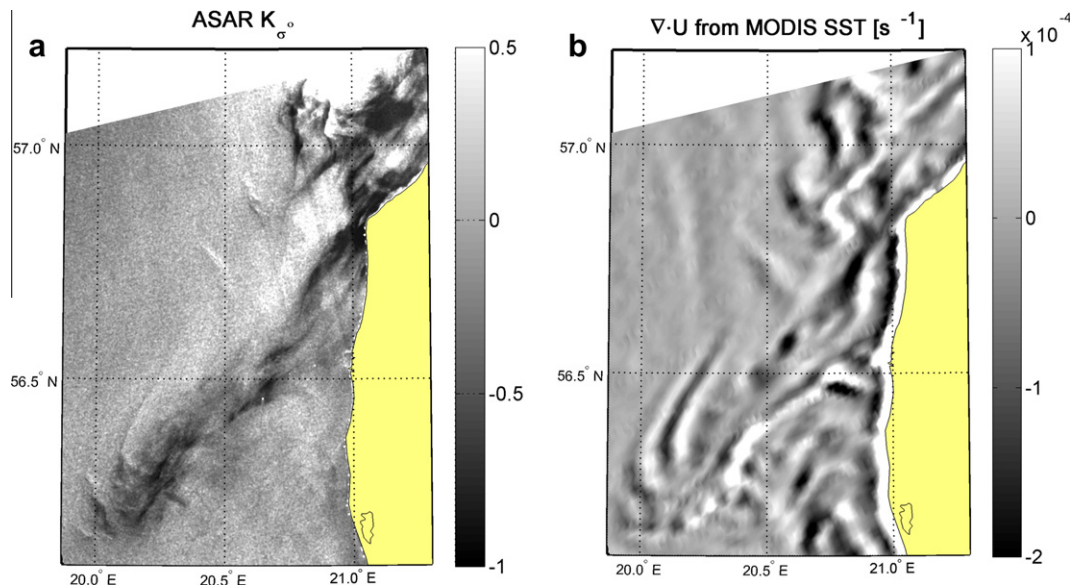


Fig. 12. (a) The radar backscatter contrasts and (b) the field of the surface current divergence reconstructed from the corresponding SST field and SAR wind data from the 16 July 2006 event.

produce rather complex SAR signatures of the upwelling zone at favorable low wind speed conditions.

5. Conclusions

Analysis of the concurrent ASAR NRCS and MODIS SST images of the SE Baltic Sea showed that the observed dark anomalies in the SAR images are attributed to the manifestation of the cold upwelling waters. Unlike the SST fields derived from IR imagery, the ASAR data provides valuable information on the location of the thermal front under cloudy conditions. Moreover, under favorable low wind speed conditions the SAR also captures the finer structures of the upwelling front at the order of 2–5 km with the corresponding SST drops of just 1–2 °C.

A quantitative interpretation of the SAR image expressions was executed by model simulations of the MABL transformation over the SST front. The SST difference across the front leads to changes in the MABL stratification and, in turn, changes in the near surface wind speed and wind stress and hence the radar backscatter (calculated from the CMOD4 model). All in all the model simulations of the radar backscatter patterns are in a good agreement with the SAR observations.

In particular, it is found that the SAR image contrasts (in dB) over the SST front can be related to the dimensionless stratification parameter $\mu_f = \kappa^2(g/T_K) \cdot \Delta\theta_s/fU_{10}$ based on the 10-m wind speed on the upwind side of the front and the SST difference across the front. This empirical relationship is consistent with the general finding of the MABL transformation over the abrupt change in the surface temperature. The maximum observed suppression of the SAR signal over the cold water was about –10 dB. However, the magnitude of the SAR backscatter anomalies over the SST front attenuates rapidly with the increase of the wind speed and the decrease of the SST difference across the front. Following the empirical relationship, a “reliable” SAR detection of the SST front with $\Delta\theta_s$ varying from 2 °C to 10 °C (assuming that the NRCS difference over a front should exceed $\Delta\sigma^\circ = -3$ dB) is possible at low to moderate wind speeds.

It is moreover found that the suppression of the radar backscatter by the presence of surface films plays an important role in the SAR image manifestation of the upwelling zones. Dark narrow and elongated SAR backscatter features are associated with the suppression of the short waves by the surfactants accumulated in the zones of the surface current convergence. This was documented by the reconstruction of the surface current convergence field from the MODIS SST and SAR wind fields.

In summary the combined effect of the MABL stratification and the effect of the short wave damping by the surfactants accumulating in the surface current convergence produces rather complex SAR signatures of the upper ocean upwelling dynamics in the coastal zone. However, under favorable wind conditions the SAR data reveal promising capabilities to detect and monitor coastal

upwelling zones with high spatial resolution regardless of the cloud conditions.

Acknowledgments

The authors would like to acknowledge the support from Mega-grant of the Russian Federation Government to support scientific research under the supervision of leading scientist at Russian State Hydrometeorological University, No. 11.G34.31.0078; YGGDRASIL fellowship granted by Norwegian Research Council under the project No. 195724/V11; the grant of the President of the Russian Federation for study and research abroad for 2010/2011; the Federal Goal-Oriented Programme under the contract N14.740.11.0201, and Research Council of Lithuania.

References

- Askari, F., Geernaert, G.L., Keller, W.C., et al. Radar imaging of thermal fronts. *Int. J. Remote Sens.* 14, 275–294, 1993.
- Beal, R.C., Katz, I., DeLeonibus, P. (Eds.). *Spaceborne SAR for Oceanography*. The Johns Hopkins University Press, Baltimore, 1981.
- Beal, R., Kudryavtsev, V., Thompson, D., et al. The influence of the marine atmospheric boundary layer on ERS-1 synthetic aperture radar imagery of the Gulf Stream. *J. Geophys. Res.* 102 (C3), 5799–5814, 1997.
- Brown, O.B., Minnett, P.J. MODIS Infrared Sea Surface Temperature Algorithm. University of Miami, Tech. Report ATBD25, FL 33149-1098, Miami, 1999.
- Brown, R. On two layer models and the similarity functions for the PBL. *Boundary Layer Meteorol.* 24, 451–463, 1982.
- Bychkova, I., Viktorov, S. Use of satellite data for identification and classification of upwelling in the Baltic Sea. *Oceanology* 27 (2), 158–162, 1987.
- Clemente-Colon, P., Yan, X.-H. Low backscatter features in SAR imagery. *JHU APL Tech. Digest.* 21 (1), 116–121, 2000.
- Espedal, H.A., Johannessen, O.M., Johannessen, J.A., Dano, E., Lyzenga, D.R., Knulst, J.C. COASTWATCH'95: ERS 1/2 SAR detection of natural film on the ocean surface. *J. Geophys. Res.* 103 (C11), 24,969–24,982, 1998.
- Isern-Fontanet, J., Lapeyre, G., Klein, P., et al. Three-dimensional reconstruction of oceanic mesoscale currents from surface information. *J. Geophys. Res.* 113, C09005, doi:10.1029/2007JC004692, 2008.
- Johannessen, J.A., Shuchman, R.A., Johannessen, O.M. Synthetic aperture radar imaging of upper ocean circulation features and wind fronts. *J. Geophys. Res.* 96 (C6), 10411–10422, 1991.
- Johannessen, J., Shuchman, R., Digranes, G., et al. Coastal ocean fronts and eddies imaged with ERS-1 synthetic aperture radar. *J. Geophys. Res.* 101 (C3), 6651–6667, 1996.
- Johannessen, J.A. Coastal observing systems: the role of synthetic aperture radar. *JHU APL Tech. Digest.* 21 (1), 1–14, 2000.
- Johannessen, J.A., Kudryavtsev, V., Akimov, D., et al. On radar imaging of current features: 2. Mesoscale eddy and current front detection. *J. Geophys. Res.* 110, C07017, doi:10.1029/2004JC002802, 2005.
- Klein, P., Hua, B. The mesoscale variability of the sea surface temperature: An analytical and numerical model. *J. Mar. Res.* 48, 729–763, 1990.
- Kowalewski, M., Ostrowski, M. Coastal up- and downwelling in the southern Baltic. *Oceanologia.* 47 (4), 453–475, 2005.
- Kreżel, A., Ostrowski, M., Szymelfenig, M. Sea surface temperature distribution during upwelling along the Polish Baltic coast. *Oceanologia* 47 (4), 415–432, 2005.
- Kudryavtsev, V.N., Grodsky, S.A., Dulov, V.A., Malinovsky, V.V. Observations of atmospheric boundary layer evolution above the Gulf Stream frontal zone. *Boundary-Layer Meteorol.* 79, 51–82, 1996.

- Kudryavtsev, V.N., Malinovsky, V.V., Rodin, A.V. Manifestation of temperature fronts in radar images of ocean. *Issled. Zemli iz Kosmosa* 6, 16–26 (In Russian), 1999.
- Kudryavtsev, V., Akimov, D., Johannessen, J., Chapron, B. On radar imaging of current features: 1. Model and comparison with observations. *J. Geophys. Res.* 110, C07016, doi:10.1029/2004JC002505, 27p, 2005.
- Kudryavtsev, V., Myasoedov, A., Chapron, B., et al. Synergy of SAR and optical imagery in studies of meso-scale ocean dynamics, in: *Proc. SeaSAR 2010*. ESA SP-679, ESA Publications Division, p. 8, 2010.
- Kudryavtsev, V., Myasoedov, A., Chapron, B., Johannessen, J.A., Collard, F. Imaging meso-scale upper ocean dynamics using SAR and optical data. *J. Geophys. Res.*, submitted for publication.
- Lehmann, A., Myrberg, K. Upwelling in the Baltic Sea – a review. *J. Mar. Syst.* 74, S3–S12, 2008.
- Marmorino, G.O., Jansen, R.W., Valenzuela, G.R., et al. Gulf Stream surface convergence imaged by synthetic aperture radar. *J. Geophys. Res.* 99, 18315–18328, 1994.
- Siegel, H., Gerth, M., Tschersich, G. Sea surface temperature development of the Baltic Sea in the period 1990–2004. *Oceanologia* 48 (S), 119–131, 2006.
- Smith, S.D. Coefficients for the sea surface wind stress, heat flux, and wind profiles as a function of wind speed and temperature. *J. Geophys. Res.* 93, 15467–15472, 1988.
- Stoffelen, A., Anderson, D. Scatterometer data interpretation: estimation and validation of the transfer function CMOD4. *J. Geophys. Res.* 102 (C3), 5767–5780, 1997.
- Suursaar, U., Aps, R. Spatio-temporal variations in hydro-physical-chemical parameters during a major upwelling event off the southern coast of the Gulf of Finland in summer 2006. *Oceanologia* 49 (2), 209–228, 2007.
- Uibopin, R., Laanemets, J. Upwelling characteristics derived from satellite sea surface temperature data in the Gulf of Finland, Baltic Sea. *Boreal Environ. Res.* 14, 297–304, 2009.
- Weissmann, D.E., Tompson, T.W., Legeckis, R. Modulation of sea surface radar cross section by surface stress: wind speed and temperature effects across the Gulf Stream. *J. Geophys. Res.* 85 (C9), 5032–5042, 1980.
- Zhubas, V.M., Stipa, T., Mälkki, P., et al. Mesoscale variability of upwelling in the southeast Baltic: infrared images and numerical modeling. *Oceanology* 44, 495–504, 2004.